ORIGINAL PAPER

Jaemin Shin · Junxiang Yang · Chaeyoung Lee ·
Junseok Kim

The Navier–Stokes–Cahn–Hilliard model with a high-order polynomial free energy

Abstract In this paper, we present a high-order polynomial free energy for the phase-field model of two-phase incompressible fluids. The model consists of the Navier–Stokes (NS) equation and the Cahn–Hilliard (CH) equation with a high-order polynomial free energy potential. In practice, a quartic polynomial has been used for the bulk free energy in the CH equation. It is well known that the CH equation does not satisfy the maximum principle and the phase-field variable takes shifted values in the bulk phases instead of taking the minimum values of the double-well potential. This phenomenon substantially changes the original volume enclosed by the isosurface of the phase-field function. Furthermore, it requires fine resolution to keep small shapes. To overcome these drawbacks, we propose high-order (higher than fourth order) polynomial free energy potentials. The proposed model is tested for an equilibrium droplet shape in a spherical symmetric configuration and a droplet deformation under a simple shear flow in a fully three-dimensional fluid flow. The computational results demonstrate the superiority of the proposed model with a high-order polynomial potential to the quartic polynomial function in volume conservation property.

1 Introduction

In the natural world or industrial fields, multi-phase flow phenomena are very common and their applications are also important. In nature, the Rayleigh–Taylor instability (RTI) and Kelvin–Helmholtz instability (KHI) are two famous phenomena of fluid interfacial instability; the RTI occurs when the heavier fluid locates upon a lighter one, and then the disturbance on the interface grows in time. This phenomenon can be used to interpret the phenomena of supernova explosions, supernova remnants, nuclear weapon explosions, etc. For the simulations of RTI, please refer to [1]. The HKI usually occurs when the velocity difference exists on the interface. In the HKI, the interface deforms and evolves into a spiral. One typical application of this phenomenon is to explain the formation of a billow cloud. See [2] for the simulations of two-phase and multi-phase KHI. Another important multi-phase fluid instability is called the Rayleigh–Plateau instability (RPI), where the surface tension is a dominant disturbing force. The RPI can explain the formation of droplets from a liquid film, and it also works during the single or double emulsion formations [3,4]. Moreover, the droplet dynamics also belongs to the category of multi-phase flow with interfacial deformation. Recently, many works have been done to model or simulate the problems related to the droplet dynamics. Hua et al. [5] used the immersed boundary method to investigate the side wall effect on the single droplet deformation in shear flow and also studied the compound droplet deformation in shear flow [6]. In turbulent flow, Soligo et al. [7] used

J. Shin
Institute of Mathematical Sciences, Ewha Womans University, Seoul 03760, Republic of Korea

J. Yang · C. Lee · J. Kim (✉)
Department of Mathematics, Korea University, Seoul 02841, Republic of Korea
E-mail: cfdkim@korea.ac.kr

the phase-field model to study the breakup and coalescence dynamics of the surfactant-laden droplet. By using the volume-of-fluid method, Lunkad et al. [8] investigated the dynamics of droplet impact and spreading on a slant solid plane. In the phase-field method, the topology change of interface can be implicitly captured by solving the governing equation. We note that the Cahn–Hilliard–Navier–Stokes system is one of the popular models in the phase-field method, where the mass conservation can be naturally satisfied. Recently, Song et al. [9] have extended the Cahn–Hilliard–Navier–Stokes model to study the core-annular pipe flow.

In this study, we investigate the effect of a high-order polynomial free energy on the dynamics of the Cahn–Hilliard (CH) equation [10,11]. The CH equation is given as

$$\frac{\partial \phi}{\partial t}(\mathbf{x}, t) = \Delta \mu(\mathbf{x}, t), \quad \mathbf{x} \in \Omega, t > 0, \tag{1}$$

$$\mu(\mathbf{x}, t) = F'(\phi(\mathbf{x}, t)) - \epsilon^2 \Delta \phi(\mathbf{x}, t), \tag{2}$$

$$\mathbf{n} \cdot \nabla \phi(\mathbf{x}, t) = \mathbf{n} \cdot \nabla \mu(\mathbf{x}, t) = 0, \quad \mathbf{x} \in \partial \Omega, \tag{3}$$

where the order parameter $\phi(\mathbf{x}, t)$ is the difference of two concentrations in a binary mixture in a domain $\Omega \subset \mathbb{R}^d$, ($d = 1, 2, 3$). $F(\phi)$ is the free energy density, ϵ is a positive parameter related to the interfacial thickness, and $\mathbf{n}$ is the outward normal vector at the boundary. The CH equation was first introduced to model phase separation phenomenon in binary alloys [10,11]. Recently, many researchers have proposed some novel numerical schemes for solving the CH equation [12–14]. We note that the CH equation can be derived from the following total energy functional:

$$\mathcal{E}(\phi) = \int_\Omega \left[F(\phi) + \frac{\epsilon^2}{2} |\nabla \phi|^2 \right] d\mathbf{x}. \tag{4}$$

See the review paper [15] for the physical, mathematical, and numerical derivations of the CH equations. For the basic principles and practical applications of the CH equation, see [16]. In the original model for the total free energy functional, the following logarithmic free energy was used:

$$F(\phi) = \frac{\theta}{2} \left[(1 + \phi) \ln \left(\frac{1 + \phi}{2} \right) + (1 - \phi) \ln \left(\frac{1 - \phi}{2} \right) \right] + \frac{\theta_c}{2} (1 - \phi^2), \tag{5}$$

where θ and θ_c are the absolute and the critical temperatures, respectively (see Fig. 1a). However, for computational efficiency, a quartic polynomial approximation $F(\phi) = 0.25(\phi^2 - 1)^2$ has been used for replacing the logarithmic free energy function, which has singularities at $\phi = \pm 1$. From Eq. (2), we note that the value of $F'(\phi)$ is needed in actual applications. In Fig. 1c, we plot the results of $F'(\phi)$ in logarithmic form (solid line) and quartic polynomial form (open circle) and we can find that the first derivative of the quartic polynomial functional is indeed a good approximation even if the logarithmic and polynomial potential functionals $F(\phi)$ have some differences.

The CH equation has been applied to modeling and simulation for phase separation, medical image processing, diblock copolymers, two-phase flows, tumor growth, microstructures with elastic inhomogeneity, and topology optimization [17]. In particular, in this study, we focus on the multi-phase fluid flows using the CH equation. The CH equation was used in modeling two-phase fluid flows with isogeometric analysis [18], nematic liquid crystals [19], binary-fluid turbulence [20,21], quasi-incompressible system [22], ferrofluid [23], fluid-surfactant system [24], 3D patterned substrate wetting problem [25], fluid-structure interactions [26], a droplet impacting a solid surface [27], droplet formation in microfluidic flow [27], and viscoelastic fluids [28]. In all of the above-mentioned models, the quartic polynomial free energy function was used.

However, as pointed out by Yue et al. [29], if we use the quartic polynomial free energy function, then drops with an initial radius below a critical radius will disappear. Furthermore, the total energy can be reduced by shrinking the drop while simultaneously shifting the bulk phase values from the initial equilibrium minimum values. To resolve these problems, in this paper, we propose a high-order polynomial free energy:

$$F(\phi) = 0.25(\phi^m - 1)^2, \tag{6}$$

where m is an even integer. Figure 1b shows the polynomial free energy, $F(\phi) = 0.25(\phi^m - 1)^2$ for $m = 2, 4, 6,$ and 20. As the value of m increases, the bulk free energy steeply penalizes the shifting from the local minimum values. The main purpose of this article is to investigate the effect of a high-order polynomial free energy on the dynamics of the CH equation.

This paper is organized as follows. In Sect. 2, we describe the numerical solution algorithms of the spherically symmetric CH equation. In Sect. 4, we describe the numerical solution algorithms of the fully three-dimensional Navier–Stokes–Cahn–Hilliard (NSCH) system. Finally, conclusions are drawn in Sect. 5.
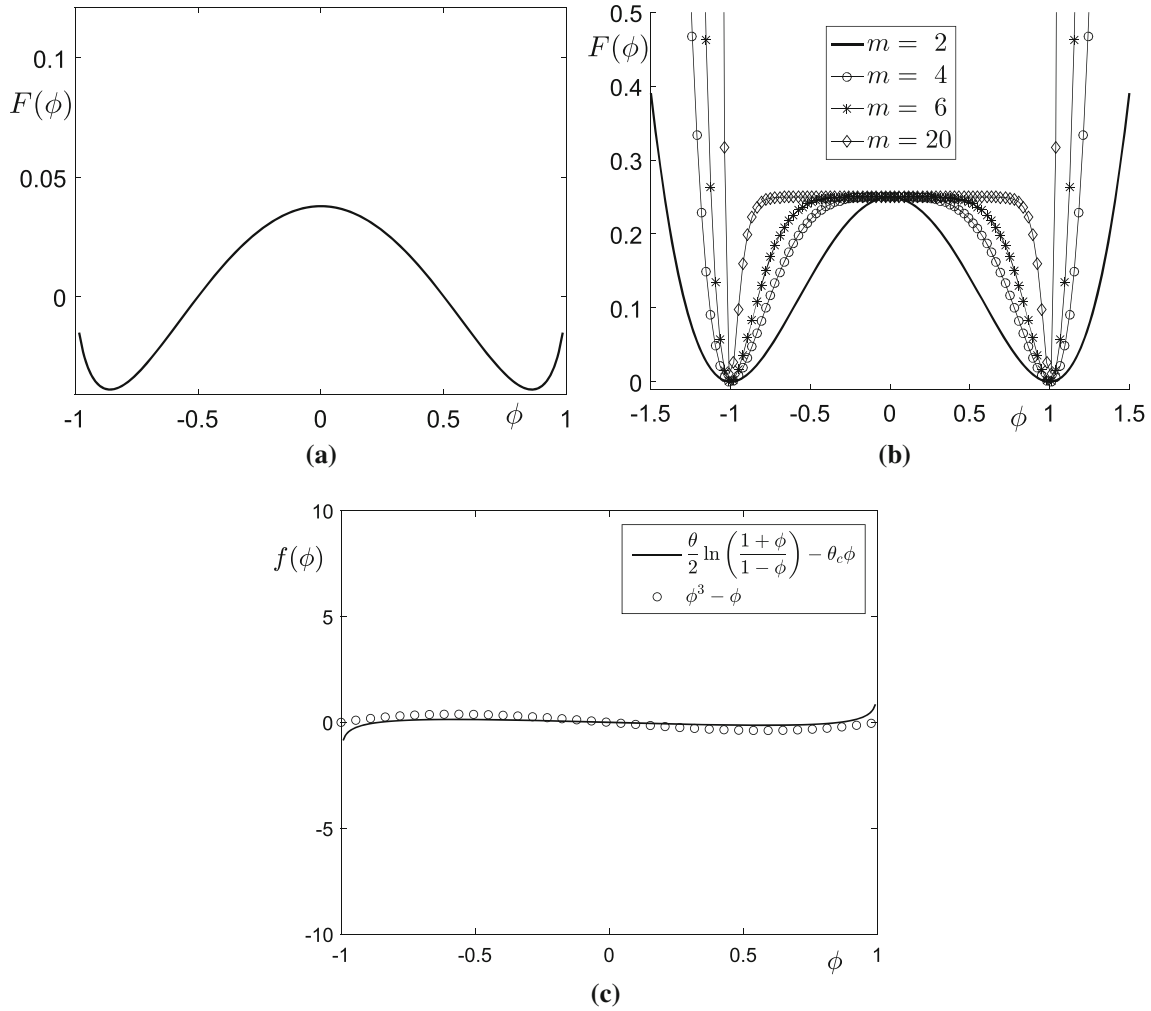
Fig. 1 **a** Logarithmic free energy with $\theta = 2/3$ and $\theta_c = 1$. **b** High-order polynomial free energy functions. **c** First derivative: $f(\phi) = F'(\phi)$ of potential functional: $F(\phi)$ in logarithmic form (solid line) and polynomial form (open circle)

2 Spherically symmetric CH equation

In this section, we consider a numerical solution in spherically symmetric form of the CH equation:

$$\phi_t(r, t) = \frac{1}{r^2}[r^2 \mu_r(r, t)]_r, \quad r \in \Omega, t > 0, \tag{7}$$

$$\mu(r, t) = F'(\phi(r, t)) - \frac{\epsilon^2}{r^2}[r^2 \phi_r(r, t)]_r. \tag{8}$$

We discretize the CH equation (7) and (8) in $\Omega = (0, a)$. Let N_r be a positive even integer, $h = a/N_r$ the uniform mesh size, and $\Omega_h = \{r_i : r_i = (i - 0.5)h, 1 \leq i \leq N_r\}$ the discrete domain. Let ϕ_i^n and μ_i^n be approximations of $\phi(r_i, t^n)$ and $\mu(r_i, t^n)$, respectively. Here, $t^n = n\Delta t$ and Δt is the time step. Let us split Eq. (6) into the difference of two convex functions,

$$F(\phi) = F_c(\phi) - F_e(\phi), \tag{9}$$

where $F_c(\phi) = 0.25(\phi^{2m} + 1)$ and $F_e(\phi) = 0.5\phi^m$. Then, $F'(\phi) = F'_c(\phi) - F'_e(\phi) = 0.5m\phi^{2m-1} - 0.5m\phi^{m-1}$. Now, we discretize Eqs. (7) and (8) in time by a nonlinear splitting algorithm [30]:

Table 1 Thickness of the interface transition layer with for various m and ϵ values

Case	$\epsilon = 0.5h$	$\epsilon = h$	$\epsilon = 2h$	$\epsilon = 4h$	$\epsilon = 8h$
$m = 2$	2.3149h	4.3185h	8.4077h	17.0179h	36.7914h
$m = 4$	0.9780h	3.0569h	6.3130h	12.5800h	25.5724h
$m = 6$	0.9318h	2.8308h	5.6834h	11.4071h	23.0144h
$m = 20$	0.9024h	0.9137h	2.7742h	10.0797h	20.8595h

Here, $h = 1/128$
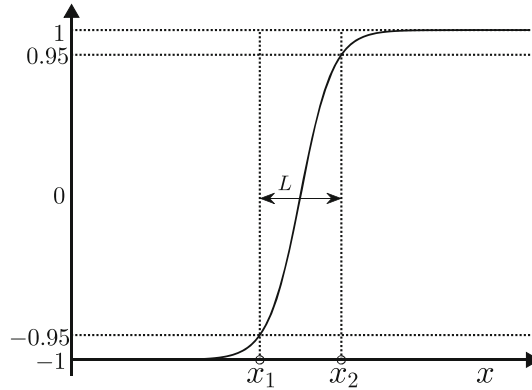
Fig. 2 The schematic diagram of the interface transition layer

$$\frac{\phi_i^{n+1} - \phi_i^n}{\Delta t} = \Delta_h \mu_i^{n+1}, \tag{10}$$

$$\mu_i^{n+1} = 0.5m(\phi_i^{n+1})^{2m-1} - 0.5m(\phi_i^n)^{m-1} - \epsilon^2 \Delta_h \phi_i^{n+1}, \tag{11}$$

where $\Delta_h \phi_i^{n+1} = [r_{i+1/2}^2(\phi_{i+1}^{n+1} - \phi_i^{n+1}) - r_{i-1/2}^2(\phi_i^{n+1} - \phi_{i-1}^{n+1})]/(r_i^2 h^2)$. The contractive term $F_c(\phi)$ and expansive $F_e(\phi)$ terms are treated implicitly and explicitly, respectively. We use the homogeneous Neumann boundary conditions for both ϕ and μ. The resulting system of discrete equations is solved by using a multi-grid method [31].

First, we study the relationship between ϵ value and thickness of interface transition layer for various m values. We take an initial condition

$$\phi(r, 0) = \begin{cases} 1 & \text{if } r \leq qh, \\ -1 & \text{otherwise} \end{cases} \tag{12}$$

in the computational domain $\Omega = (0, 1)$ with 128 grid points. Here, we use $q = 70$, $\Delta t = 0.1h^2$. Let us define a numerical equilibrium solution if the discrete l_2-norm of the difference between the two consecutive time step solutions is less than 10^{-6}, i.e., $\|\phi^{n+1} - \phi^n\|_2 < 10^{-6}$. Table 1 shows the thickness of the interface transition layer for various m and ϵ values (Fig. 2).

If we fit the data by linear functions, then we have the following equations:

$$\epsilon_2(L) = 0.2168L + 0.0009, \tag{13}$$

$$\epsilon_4(L) = 0.3080L + 0.0009, \tag{14}$$

$$\epsilon_6(L) = 0.3430L + 0.0007, \tag{15}$$

$$\epsilon_{20}(L) = 0.3541L + 0.0046. \tag{16}$$

Figure 3 shows $\epsilon_m(L)$ with respect to L with linear fitting functions for $m = 2, 4, 6$, and 20. Figure 4a shows the initial configuration with $q = 30$. Figures 4b–f show the equilibrium states with different values of q and $F(\phi) = 0.25(\phi^m - 1)^2$ for $m = 2, 4$, and 20, respectively. Here, we used $\epsilon = \epsilon_m(4h)$. From Fig. 4b, we can see that if $q = 30$, then almost constant solution is a numerical equilibrium solution. If $q = 31$, then we have a stable spherical drop solution. From Figs. 4b–f, we can confirm that the minimum number q which makes a non-flat solution decreases as m increases.
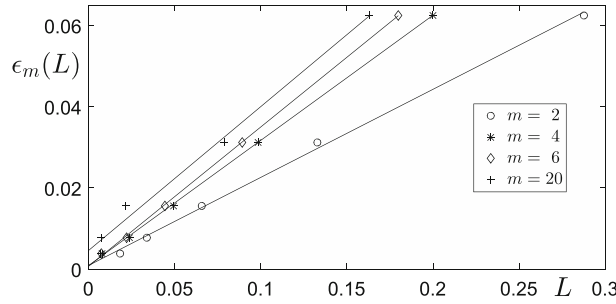
Fig. 3 $\epsilon_m(L)$ with respect to L with linear fitting functions for $m = 2, 4, 6,$ and 20
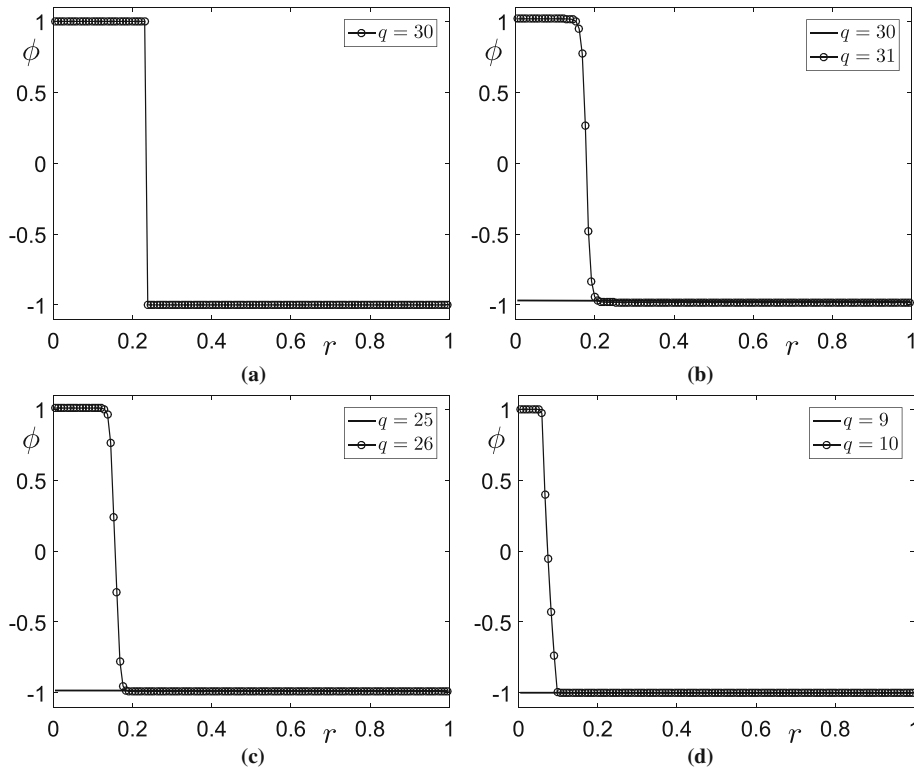
Fig. 4 **a** Initial configuration with $q = 30$. **b**, **c**, and **d** are the equilibrium sates with different values of q and $F(\phi) = 0.25(\phi^m - 1)^2$ for $m = 2, 4,$ and 20, respectively

3 Effect of exponent on the computation

In this section, we consider the effect of the exponent on the computation. For $m = 2$, the proposed scheme in Eqs. (10) and (10) is unconditionally stable, i.e., there is no blow-up even if a large time step is used. Since in the computation large exponents move the potential functional $F(\phi)$ away from the original form of double-well potential (i.e., $m = 2$), the available time step is restricted as we increase the exponent. In Table 2, we list the available maximum time steps for different exponents with different mesh sizes: $h = 1/16, 1/32, 1/64,$ and $1/128$. Note that the following initial condition is used in the two-dimensional space $\Omega = (-1, 1) \times (-1, 1)$:

$$\phi(x, y, 0) = \begin{cases} 1 & \text{if } -0.5 < x < 0.5 \text{ and } -0.5 < y < 0.5, \\ -1 & \text{otherwise.} \end{cases} \tag{17}$$

For $m = 2$ and 4, we can find that any large time step can be used. However, a smaller time step is needed if we continue to increase the exponent.

Table 2 Maximum time step for different exponents with different mesh sizes

Case	$h = 1/16$	$h = 1/32$	$h = 1/64$	$h = 1/128$
$m = 2$	∞	∞	∞	∞
$m = 4$	∞	∞	∞	∞
$m = 6$	6.25e–5	3.12e–5	1.56e–5	7.81e–6
$m = 20$	2.50e–6	1.25e–6	6.25e–7	3.12e–7
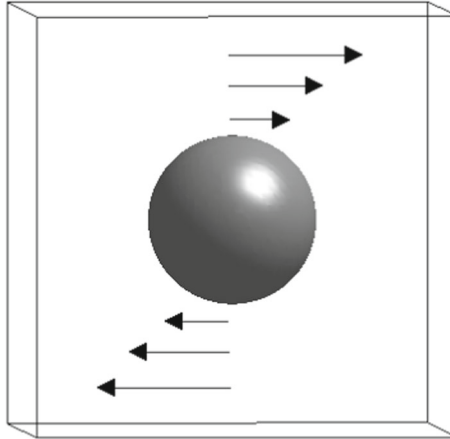
Fig. 5 The schematic diagram of a droplet in shear flow

4 Navier–Stokes–Cahn–Hilliard equations

We consider two-phase fluid flows with the high-order polynomial CH equation. The Navier–Stokes–Cahn–Hilliard (NSCH) system is

$$\mathbf{u}_t + \mathbf{u} \cdot \nabla \mathbf{u} = -\nabla p + \frac{1}{\text{Re}} \Delta \mathbf{u} - \frac{1}{2\text{We}} \nabla \cdot \left(\frac{\nabla \phi}{|\nabla \phi|} \right) \nabla \phi, \tag{18}$$

$$\nabla \cdot \mathbf{u} = 0, \tag{19}$$

$$\phi_t + \nabla \cdot (\phi \mathbf{u}) = \frac{1}{\text{Pe}} \Delta \mu, \tag{20}$$

$$\mu = F'(\phi) - \epsilon^2 \Delta \phi, \tag{21}$$

where $\mathbf{u} = (u, v, w)$ is the velocity and p is the pressure. The dimensionless parameters are the Reynolds number Re, Weber number We, and Peclet number Pe. In Eq. (18), the surface tension term can be rewritten as

$$-\frac{1}{2\text{We}} \nabla \cdot \left(\frac{\nabla \phi}{|\nabla \phi|} \right) \nabla \phi = \frac{1}{\text{We}} \nabla \cdot \left(-\frac{\nabla \phi}{|\nabla \phi|} \right) \frac{|\nabla \phi|}{2} \frac{\nabla \phi}{|\nabla \phi|}, \tag{22}$$

where $\nabla \cdot (-\nabla \phi / |\nabla \phi|)$ is the curvature, $|\nabla \phi|/2$ is the smoothed Dirac delta function [32], and $\nabla \phi / |\nabla \phi|$ is the unit normal vector to the surface. Because the profile of the interfacial transition layer with $m \geq 4$ is not hyperbolic tangent, we use $|\nabla \phi|/2$ for the smoothed Dirac delta function. Here, we view the phase-field model as a computational method and define the surface tension effect using geometric feature of the interface.

We consider a droplet evolution under simple shear flow. The schematic diagram of a droplet under shear flow is shown in Fig. 5.

4.1 Two-dimensional droplet deformation in shear flow

First, the two-dimensional droplet deformation in shear flow is investigated for different values of m. The numerical parameters are $h = 1/128$, $\Delta t = 0.005h^2$, Re $= 500$, We $= 100$. The initial condition is given as
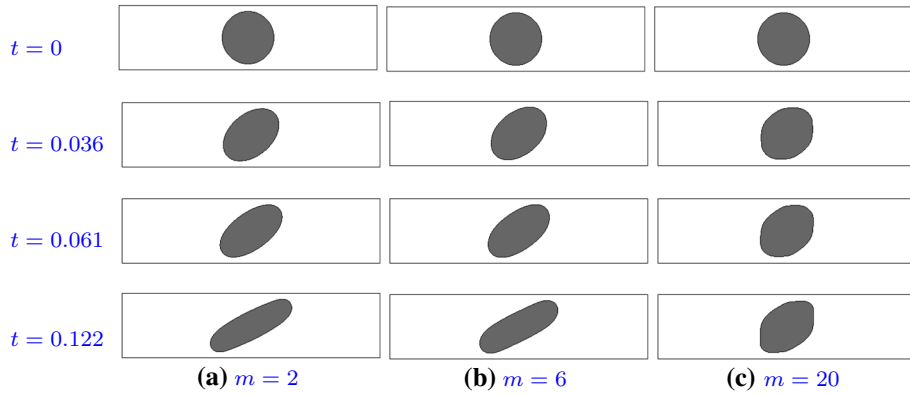
Fig. 6 Temporal evolutions of droplet for **a** $m = 2$, **b** $m = 6$, **c** $m = 20$. The dimensionless times from the top to bottom are: $t = 0, 0.036, 0.061, 0.122$
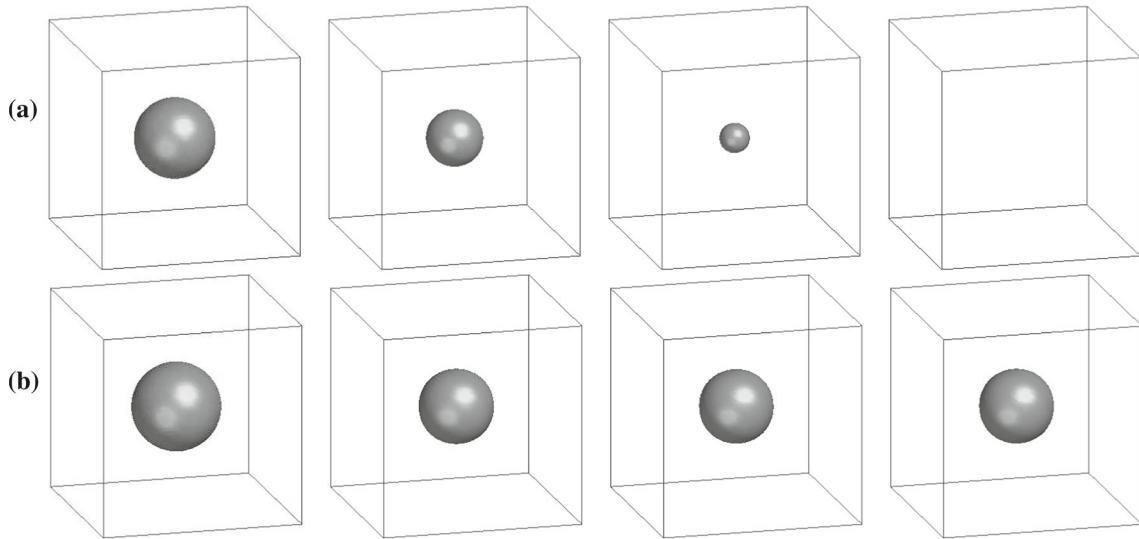
Fig. 7 Temporal evolutions of droplet with **a** $r = 0.2$ and **b** $r = 0.22$. The dimensionless times from the left to right are: $t = 0, 2.4414, 6.1035, 125.7324$

$$\phi(x, y, 0) = \tanh\left(\frac{0.2 - \sqrt{(x-1)^2 + (y-0.25)^2}}{\sqrt{2}\epsilon}\right), \tag{23}$$

$$u(x, y, 0) = 16(y - 0.25), \; v(x, y, 0) = 0, \; p(x, y, 0) = 0 \tag{24}$$

on the computational domain $\Omega = [0, 2] \times [0, 0.5]$. Figures 6a–c show the temporal evolutions of a droplet in shear flow for $m = 2, 6, 20$. We can find that the interface of the droplet becomes rough and twisted as $m = 20$.

4.2 Three-dimensional CH dynamics without flow

Next, we investigate the dynamics of the CH equation for $m = 2$, and a droplet is located in the domain $\Omega = (-0.5, 0.5) \times (-0.5, 0.5) \times (-0.5, 0.5)$ without fluid flow. Here, $h = 1/64$, $\Delta t = 100h^2$, and Pe $= 1$ are used. Figure 7 shows the temporal evolutions of droplet for different initial radii. The droplet with radius $r = 0.2$ vanishes gradually. However, the droplet with radius $r = 0.22$ exists for a long time.

To compare the equilibrium profiles under different exponents, we consider the CH dynamics without flow in three-dimensional space. The initial condition is a sphere with radius $r = 0.22$. Here, different exponents ($m = 2, 4, 6,$ and 20) are used to perform the simulation until the numerical equilibrium state is reached. The
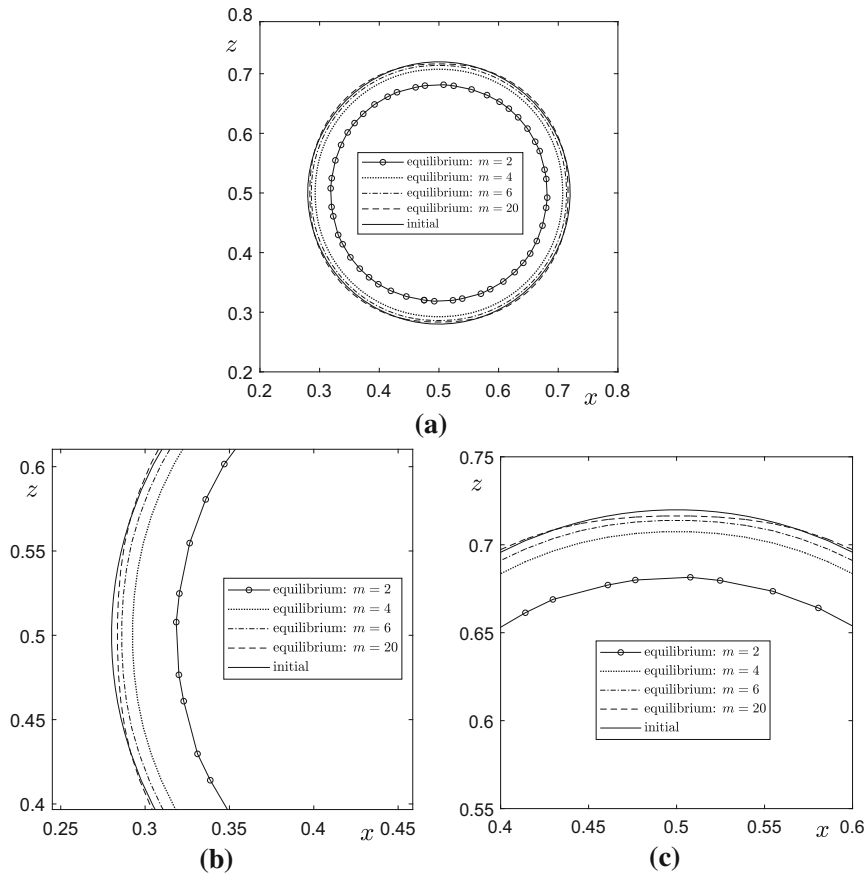
Fig. 8 Equilibrium profiles at $y = 0$ with respect to different exponents

equilibrium profiles at $y = 0$ are illustrated in Fig. 8a, and Figs. 8b, c show the locally enlarged views at the right end and the top end, respectively. Here, the solid line represents the initial profile; the dashed line, dash-dotted line, dotted line, and the line with circle markers are the equilibrium profiles with $m = 20, 6, 4$, and 2, respectively. As we can observe, the shrinking of the droplet is suppressed as the exponent increases. However, a much larger exponent ($m = 20$) leads to a non-circular profile. Therefore, the exponent $m = 6$ is a proper choice.

### 4.3 Three-dimensional droplet deformation in shear flow

We consider the shear flow governed by the NSCH system on the computational domain $\Omega = (-1, 1) \times (-0.5, 0.5) \times (-0.5, 0.5)$. The parameters used are $h = 1/64$, $\Delta t = 5h^2$, Re $= 500$, and We $= 100$. We take the following initial condition:

$$\phi(x, y, z, 0) = \tanh\left(\frac{0.22 - \sqrt{x^2 + y^2 + z^2}}{\sqrt{2}\epsilon}\right),$$

$$(u, v, w) = (z, 0, 0).$$

Figure 9 shows the temporal evolution of the droplet under simple shear flow in three-dimensional space. In this test, we use $\epsilon = \epsilon_m(4h)$ and Pe $= 1/\epsilon_4(4h)$. Figures 9a–c represent the results with $m = 2, 6$, and 20, respectively. We can find that the droplet with $m = 2$ is vanishing as time evolves. Meanwhile, the droplets with $m = 6, 20$ always exist. Next, we check the temporal evolution of the discrete volume of a droplet with different m values. The detailed definition of the discrete volume can be found in [33]. Figure 10 shows the temporal evolution of the discrete volume of a droplet, and we can find that a larger m value effectively prevents the decrease in the discrete volume of the droplet. In the two-dimensional case, we found that the interface of the droplet will become rough and twisty with $m = 20$. Although the volume can be better conserved with
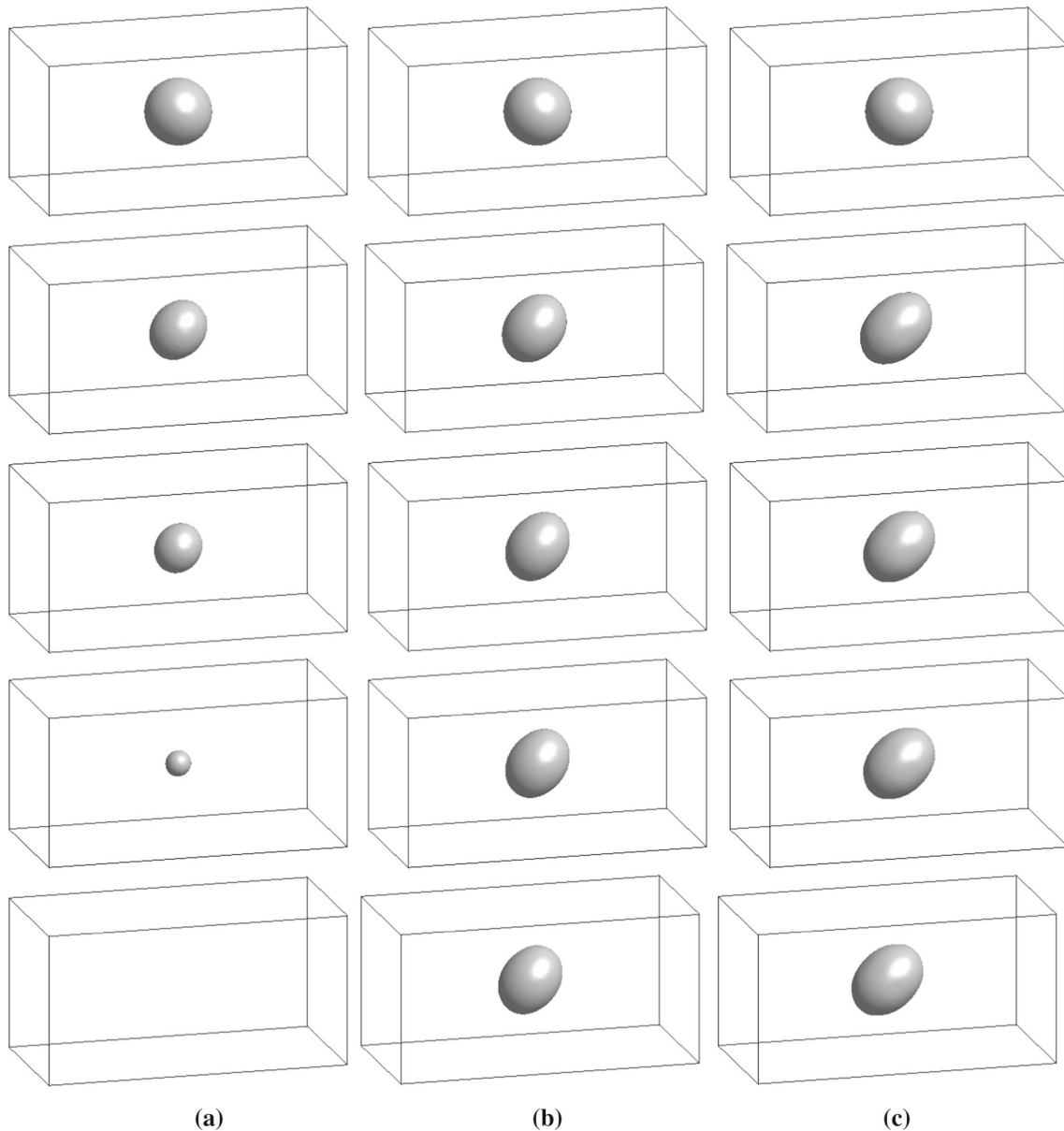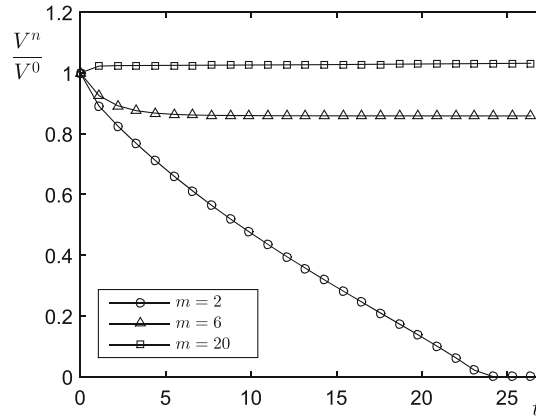
Fig. 9 Temporal evolutions of droplet for **a** $m = 2$, **b** $m = 6$, and **c** $m = 20$. The dimensionless times from the top to bottom are: $t = 0, 6.1035, 12.2070, 21.3623, 30.5176$

$m = 20$, the rough interface can also be found in Fig. 11c. Moreover, we can find that the evolution is delayed with $m = 20$ by comparing the results in Figs. 11a–c; therefore, $m = 6$ is a better choice for the simulation.

We should note that the disappearance of small drops is not necessarily wrong, as it is experimentally observed that drops must be larger than a certain minimum size; otherwise, they are reabsorbed into the surrounding continuous phase. Nevertheless, the phase-field model emphasizes this effect too much; together with the fact that the composition inside a drop remains too far from its equilibrium value, this effect is attributed to non-equilibrium surface tension, see [34] for more details.

4.4 Comparison with Taylor's theory

Here, we consider the three-dimensional droplet deformation in shear flow. This is a classical problem that was solved analytically in the creeping flow condition by Taylor [35], and he found that when the droplet arrives at

Fig. 10 Temporal evolutions of the discrete volume of a droplet for $m = 2, 6,$ and 20
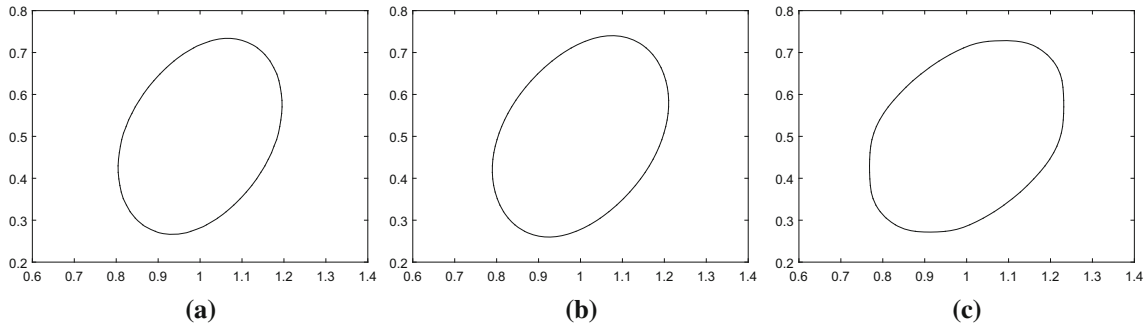
Fig. 11 The cross-profiles of three-dimensional droplet at $t = 2.7466$ for **a** $m = 2$, **b** $m = 6$, and **c** $m = 20$
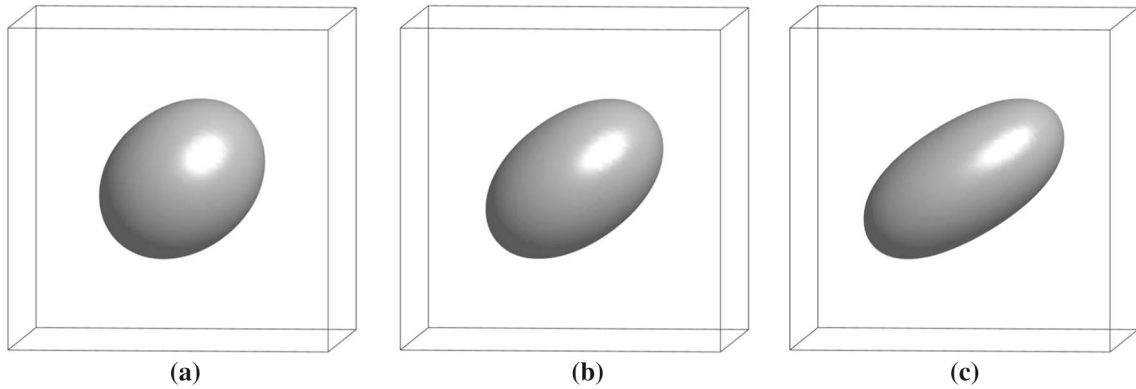
Fig. 12 Snapshots of droplet at equilibrium state with respect to different capillary numbers: **a** Ca $= 0.1$, **b** Ca $= 0.2$, **c** Ca $= 0.3$

the dynamics equilibrium state, i.e., the externally imposed shear flow balances with the interface relaxation, the deformation parameter $D = (L + B)/(L - B)$ is related to the capillary number Ca $= \eta\gamma r/\sigma$, where L and B are the maximum and minimum deformation length, respectively, η is the viscosity of the ambient fluid, γ is the local shear rate, r is the radius of the droplet, and σ is the surface tension coefficient. Later, Shapira and Haber [36] further investigated the wall effects on the droplet deformation in the low Reynolds condition. In this work, we compare the numerical results with the following Taylor formula:

$$D = \frac{19\lambda + 16}{16\lambda + 16}\text{Ca},\tag{25}$$

Table 3 Comparisons of deformation parameter D obtained by Taylor's theory and numerical simulation

Case	Ca = 0.1	Ca = 0.2	Ca = 0.3
Taylor's theory	0.1094	0.2188	0.3281
Numerical results	0.1138	0.2186	0.3288

where λ is the viscosity ratio. In the simulation, we consider the following initial conditions:

$$\phi(x, y, z, 0) = \tanh\left(\frac{0.5 - \sqrt{x^2 + y^2 + z^2}}{\sqrt{2}\epsilon}\right), \tag{26}$$

$$u(x, y, z, 0) = z, v(x, y, z, 0) = w(x, y, z, 0) = 0 \tag{27}$$

in the domain $\Omega = (-1, 1) \times (-1, 1) \times (-1, 1)$. The numerical parameters: $h = 1/32$, $\Delta t = h^2$, $m = 6$, $\epsilon = \epsilon_6(4h)$, $\eta = 1$, $\gamma = 1$, $\lambda = 1$, and $Pe = 1/\epsilon_4(4h)$ are used. The simulations for Ca = 0.1, 0.2, and 0.3 are computed until the numerical equilibrium state is reached. Figures 12a–c show the snapshots of the droplet at equilibrium states with Ca = 0.1, 0.2, and 0.3, respectively. Table 3 illustrates comparisons of the deformation parameter obtained by Taylor's theory and numerical simulation. We can find that the numerical results and analytical results are in good agreement.

5 Conclusions

In this work, we presented a high-order polynomial free energy for the NSCH system in simulating two-phase, incompressible flow. In the classical NSCH system, to study droplet dynamics, the initial droplet radius has to be larger than a critical radius in order to get a non-vanishing result. The proposed new model reduces this limit in the same condition. The numerical results showed the effectiveness of the proposed method. In the test of the spherically symmetric CH equation, a small m value needs a large q value to get a non-flat solution, while the limited q value becomes smaller when we choose a larger m value. Moreover, the treatment of our method is simple because it only needs to increase the parameter m value to achieve the modification. The new model can be used in many application areas using the phase-field method, such as the compound droplet deformation, bubble falling and raising, droplet motion in a capillary device and a droplet impacting a solid surface. In future work, the proposed model can also be used in the Lattice–Boltzmann method for the CH equation [37–40]. Regular mixtures have a log-dependent free energy, such as Eq. (5). Then, in the vicinity of the critical point, it can be expanded in power series, obtaining a quartic polynomial. This is particularly important for van der Waals fluids because Landau's phase field is a generalization of van der Waals' theory [41]. However, if we want to model a polymer blend, then the free energy must include the degree of polymerization [42], and we may apply the proposed high-order polynomial free energy. This would be another interesting future work.

References

1. Lee, H.G., Kim, J.: On the long time simulation of the Rayleigh–Taylor instability. Int. J. Numer. Methods Eng. **85**, 1633–1647 (2011)
2. Lee, H.G., Kim, J.: Two-dimensional Kelvin–Helmholtz instabilities of multi-component fluids. Eur. J. Mech. B Fluids **49**, 77–88 (2015)
3. Mu, K., Li, E., Xu, R.X., Ding, H.: Numerical study on droplet generation in axisymmetric flow focusing upon actuation. Phys. Fluids **30**, 012111 (2018)
4. Park, J.M., Anderson, P.D.: A ternary model for double-emulsion formation in a capillary microfluidic device. Lab Chip **12**, 2672–2677 (2012)
5. Hua, H., Li, Y., Shin, J., Song, H.K., Kim, J.: Effect of confinement on droplet deformation in shear flow. Int. J. Comput. Fluid Dyn. **27**, 317–331 (2013)

6. Hua, H., Shin, J., Kim, J.: Dynamics of a compound droplet in shear flow. Int. J. Heat Fluid Flow **50**, 63–71 (2014)
7. Soligo, G., Roccon, A., Soldati, A.: Breakage, coalescence and size distribution of surfactant-laden droplets in turbulent flow. J. Fluid Mech. **881**, 244–282 (2019)
8. Lunkad, S.F., Buwa, V.V., Nigam, K.D.P.: Numerical simulations of drop impact and spreading on horizontal and inclined surfaces. Chem. Eng. Sci. **62**, 7214–7224 (2007)
9. Song, B., Plana, C., Lopez, J.M., Avila, M.: Phase-field simulation of core-annular pipe flow. Int. J. Multiph. Flow **117**, 14–24 (2019)
10. Cahn, J.W., Hilliard, J.E.: Free energy of a non-uniform system I. Interfacial free energy. J. Chem. Phys. **28**, 258–267 (1958)
11. Cahn, J.W.: Free energy of a nonuniform system II: Thermodynamic basis. J. Chem. Phys. **30**, 1121–1124 (1959)
12. Mu, Z., Gong, Y., Cai, W., Wang, Y.: Efficient local energy dissipation preserving algorithms for the Cahn–Hilliard equation. J. Comput. Phys. **374**, 654–667 (2018)
13. Du, Q., Ju, L., Li, X., Qiao, Z.: Stabilized linear semi-implicit schemes for the nonlocal Cahn–Hilliard equation. J. Comput. Phys. **363**, 39–54 (2018)
14. Chen, Y., Lowengrub, J., Shen, J., Wang, C., Wise, S.: Efficient energy stable schemes for isotropic and strongly anisotropic Cahn–Hilliard systems with the Willmore regularization. J. Comput. Phys. **365**, 56–73 (2018)
15. Lee, D., Huh, J.Y., Jeong, D., Shin, J., Yun, A., Kim, J.: Physical, mathematical, and numerical derivations for the Cahn–Hilliard equations. Comput. Mater. Sci. **81**, 216–225 (2014)
16. Kim, J., Lee, S., Choi, Y., Lee, S.-M., Jeong, D.: Basic principles and practical applications of the Cahn–Hilliard equation. Math. Probl. Eng. Article ID 9532608, 11 pages (2016)
17. Hosseini, B.S., Turek, S., Mller, M., Palmes, C.: Isogeometric analysis of the Navier–Stokes–Cahn–Hilliard equations with application to incompressible two-phase flows. J. Comput. Phys. **348**, 171–194 (2017)
18. Zhao, J., Wang, Q., Yang, X.: Numerical approximations to a new phase field model for two phase flows of complex fluids. Comput. Methods Appl. Mech. Eng. **310**, 77–97 (2016)
19. Perlekar, P., Pal, N., Pandit, R.: Two-dimensional turbulence in symmetric binary-fluid mixtures: coarsening arrest by the inverse cascade. Sci. Rep. **7**, 44589 (2017)
20. Guo, Z., Lin, P., Lowengrub, J., Wise, S.M.: Mass conservative and energy stable finite difference methods for the quasi-incompressible Navier–Stokes–Cahn–Hilliard system: primitive variable and projection-type schemes. Comput. Methods Appl. Mech. Eng. **326**, 144–174 (2017)
21. Soligo, G., Roccon, A., Soldati, A.: Mass-conservation-improved phase field methods for turbulent multiphase flow simulation. Acta Mech. **230**(2), 683–696 (2019)
22. Nochetto, R.H., Salgado, A.J., Tomas, I.: A diffuse interface model for two-phase ferrofluid flows. Comput. Methods Appl. Mech. Eng. **309**, 497–531 (2016)
23. Yang, X.: Numerical approximations for the Cahn–Hilliard phase field model of the binary fluid-surfactant system. J. Sci. Comput. **74**(3), 1533–1553 (2018)
24. Xie, Y., Wodo, O., Ganapathysubramanian, B.: Incompressible two-phase flow: diffuse interface approach for large density ratios, grid resolution study, and 3D patterned substrate wetting problem. Comput. Fluids **141**, 223–234 (2016)
25. Zheng, X., Karniadakis, G.E.: A phase-field/ALE method for simulating fluid-structure interactions in two-phase flow. Comput. Methods Appl. Mech. Eng. **309**, 19–40 (2016)
26. Zhang, Q., Qian, T.Z., Wang, X.P.: Phase field simulation of a droplet impacting a solid surface. Phys. Fluids **28**(2), 022103 (2016)
27. Bai, F., He, X., Yang, X., Zhou, R., Wang, C.: Three dimensional phase-field investigation of droplet formation in microfluidic flow focusing devices with experimental validation. Int. J. Multiph. Flow **93**, 130–141 (2017)
28. Yue, P., Zhou, C., Feng, J.J., Ollivier-Gooch, C.F., Hu, H.H.: Phase-field simulations of interfacial dynamics in viscoelastic fluids using finite elements with adaptive meshing. J. Comput. Phys. **219**(1), 47–67 (2006)
29. Yue, P., Zhou, C., Feng, J.J.: Spontaneous shrinnkage of frops and mass conservation in phase-field simulations. J. Comput. Phys. **223**(1), 1–9 (2007)
30. Eyre, D.J.: An unconditionally stable one-step scheme for gradient systems. http://www.math.utah.edu/~eyre/research/methods/stable.ps. Accessed 9 Oct 2019
31. Trottenberg, U., Schüller, A., Oosterlee, C.: Multigrid. Academic Press, New York (2000)
32. Lee, H.G., Kim, J.: Regularized Dirac delta functions for phase field models. Int. J. Numer. Methods Eng. **91**(3), 269–288 (2012)
33. Jeong, D., Kim, J.: Conservative Allen–Cahn–Navier–Stokes system for incompressible two-phase fluid flows. Comput. Fluids **156**, 239–246 (2017)
34. Lamorgese, A., Mauri, R.: Phase-field modeling of interfacial dynamics in emulsion flows: nonequilibrium surface tension. Int. J. Multiph. Flow **85**, 164–172 (2016)
35. Taylor, G.I.: The deformation of emulsions in definable fields of flows. Proc. R. Soc. Lond. A **146**, 501–523 (1934)
36. Shapira, M., Haber, S.: Low Raynolds number motion of a droplet in shear flow including wall effects. Int. J. Multiph. Flow **16**(2), 305–321 (1990)
37. Zu, Y.Q., He, S.: Phase-field-based lattice Boltzmann model for incompressible binary fluid systems with density and viscosity contrasts. Phys. Rev. E **87**, 043301 (2013)
38. Liu, H., Valocchi, A.J., Zhang, Y., Kang, Q.: Lattice Boltzmann phase-field modeling of thermocapillary flows in a confined microchannel. J. Comput. Phys. **256**(1), 334–356 (2014)
39. Wang, N., Liu, H., Zhang, C.: Three-dimensional phase-field lattice Boltzmann model for incompressible multiphase flows. J. Comput. Sci. **17**(2), 340–356 (2016)
40. Derksen, J.J., Komrakova, A.E.: Multiscale simulations of sliding droplets. Acta Mech. **230**(2), 657–666 (2019)
41. Lamorgese, A., Mauri, R., Sagis, L.M.C.: Modeling soft interface dominated systems: a comparison of phase field and Gibbs dividing surface models. Phys. Rep. **675**, 1–54 (2017)

42. de Gennes, P.G.: Dynamics of fluctuations and spinodal decomposition in polymer blends. J. Chem. Phys. **72**(9), 4756–4763 (1980)